The regional scale surface mass balance of Pine Island Glacier, West Antarctica over the period 2005–2014, derived from airborne radar soundings and neutron probe measurements

Stefan Kowalewski[1], Veit Helm[1], Elizabeth Morris[2], and Olaf Eisen[1]

[1]Alfred Wegener Institute, Helmholtz Centre for Polar and Marine Research, Bremerhaven, Germany
[2]Scott Polar Research Institute, University of Cambridge, UK

Correspondence: Stefan Kowalewski (stefan.kowalewski@awi.de)

Abstract. We derive recent surface mass balance (SMB) estimates from airborne radar observations along the iSTAR traverse (2013,2014) at Pine Island Glacier (PIG), West Antarctica. Ground based neutron probe measurements of snow density at 22 locations allow us to derive SMB from the annual internal radar reflection layers. The 2005 layer was traced for a total distance of 2367 km allowing us to determine annual mean SMB for the period 2005–2014. Using complementary SMB
5 estimates from the RACMO2.3p2 regional climate model and a geostatistical kriging scheme we determine a regional scale SMB distribution with the same main characteristics as that determined for the period 1985–2009 in previous studies. Local departures exist for the northern PIG slopes, where the orographic precipitation shadow effect appears to be more pronounced in our observations, and the southward interior, where the SMB gradient is more pronounced in previous studies. For the PIG basin, we derive a total mass input of $79.9 \pm 19.2 \, \mathrm{Gt \, yr^{-1}}$. This is not significantly different to the value of $78.3 \pm 6.8 \, \mathrm{Gt \, yr^{-1}}$
10 for the period 1985–2009. Thus there is no evidence of a secular trend in mass input to the PIG basin. We note, however, that our estimated uncertainty is more than twice the uncertainty for the 1985–2009 estimates. Our error analysis indicates that uncertainty estimates on total mass input are highly sensitive to the selected krige methodology and assumptions made on the interpolation error, which we identify as the main cause for the increased uncertainty range compared to the 1985–2009 estimates.

15 ## 1 Introduction

The stability of the West Antarctic Ice Sheet (WAIS) is a major concern for scientists seeking to predict global sea level rise. Transport of heat from the upwelling circumpolar deep water has proved to be a critical driver of Antarctic ice shelf thinning and grounding line retreat, thus stimulating the acceleration of marine-terminating outlet glaciers (e.g. Hillenbrand et al., 2017). In particular the Amundsen Sea sector has experienced an unprecedented acceleration in ice discharge since the beginning of
20 satellite based ice flow observations in the 1970s. Three quarters of this ice discharge stem from the Thwaites and Pine Island glaciers with both showing evidence of rapid acceleration since the 1970s (Mouginot et al., 2014) and spreading of surface lowering along their tributaries over the past two decades (Konrad et al., 2017). While spaceborne observations indicate that this acceleration has levelled off recently (Rignot et al., 2019), they also support model projections suggesting modest changes

in mass balance, i.e. the resulting net ice loss after accounting for all loss and gain processes, for the next decades to come
25 (Bamber and Dawson, 2020). The dynamic ice loss is mainly responsible for the negative mass balance of Pine Island Glacier
(PIG). The net input is commonly referred to as the surface mass balance (SMB), i.e. snowfall minus sublimation, meltwater
runoff, and erosion/deposition of snow (Lenaerts et al., 2012; Medley et al., 2013). Various methods exist to measure the SMB
on the ground (Eisen et al., 2008). The remoteness of WAIS makes such measurements logistically challenging, in particularly
when extending these measurements to regional scales. Basin wide mass balance estimates strongly depend on the coverage
30 and quality of SMB measurements. The study of Medley et al. (2014), in the following abbreviated as ME14, presents the first
comprehensive survey of mean annual SMB between 1985 and 2009/10 from airborne radar based observations of the Thwaites
and Pine Island glaciers. They demonstrated that such airborne radar observations provide a critical means to overcome the
logistical challenges. However, these measurements rely on assumptions about the dielectric properties of snow, which include
knowledge of the vertical snow density profile. In this sense, ground-truthing measurements remain an important tool for cali-
35 brating the radar soundings.

As part of the iSTAR Ice Sheet stability programme, a traverse across the Pine Island Glacier (PIG) was carried out in 2013/14
and repeated the year after. In the following, we name the first traverse T1 and the second T2. In total 22 sites were occupied
during both traverses. Boreholes of at least 13 m depth were drilled at each site during traverse T1. Density–depth profiles
were measured with a Neutron Probe (NP) device during both traverses (Morris et al., 2017) and supplementary analysis of
40 firn cores was performed for 10 sites during traverse T2 to determine additional independent proxies related to the annual snow
accumulation (Konrad et al., 2019).

The Alfred Wegener Institute (AWI) contributed to the iSTAR traverse T2 with radar soundings from the Airborne SAR / In-
terferometric Radar Altimeter System (ASIRAS) aboard the Polar 5 research plane. Previous ASIRAS missions have demon-
strated its capability to trace annual snow accumulation layers of the upper firn column at regional scales over Greenland
45 (Hawley et al., 2006; Overly et al., 2016). The PIG flight track connects all iSTAR sites so that internal annual snow accumu-
lation layers can be traced to make regional scale SMB estimates. By comparison with earlier SMB measurements at PIG, the
vertical profiling based on the ASIRAS soundings achieves a resolution that is one order of magnitude higher (Tab. 1), which
helps to trace narrow internal snow accumulation layers. In addition, the ASIRAS flight track contains several self-intersections
so that we can compare and adjust traced layers at those points.

50 In this study we first address local departures between SMB estimates from ASIRAS and NP measurement to evaluate the
uncertainty of our regional scale ASIRAS SMB estimates. We then compare our results with those reported by ME14 and
discuss differences between both data sets. Finally, we apply our new regional scale SMB estimates to different PIG mass
balance inventories to evaluate their impact in light of the current stability of the study area.
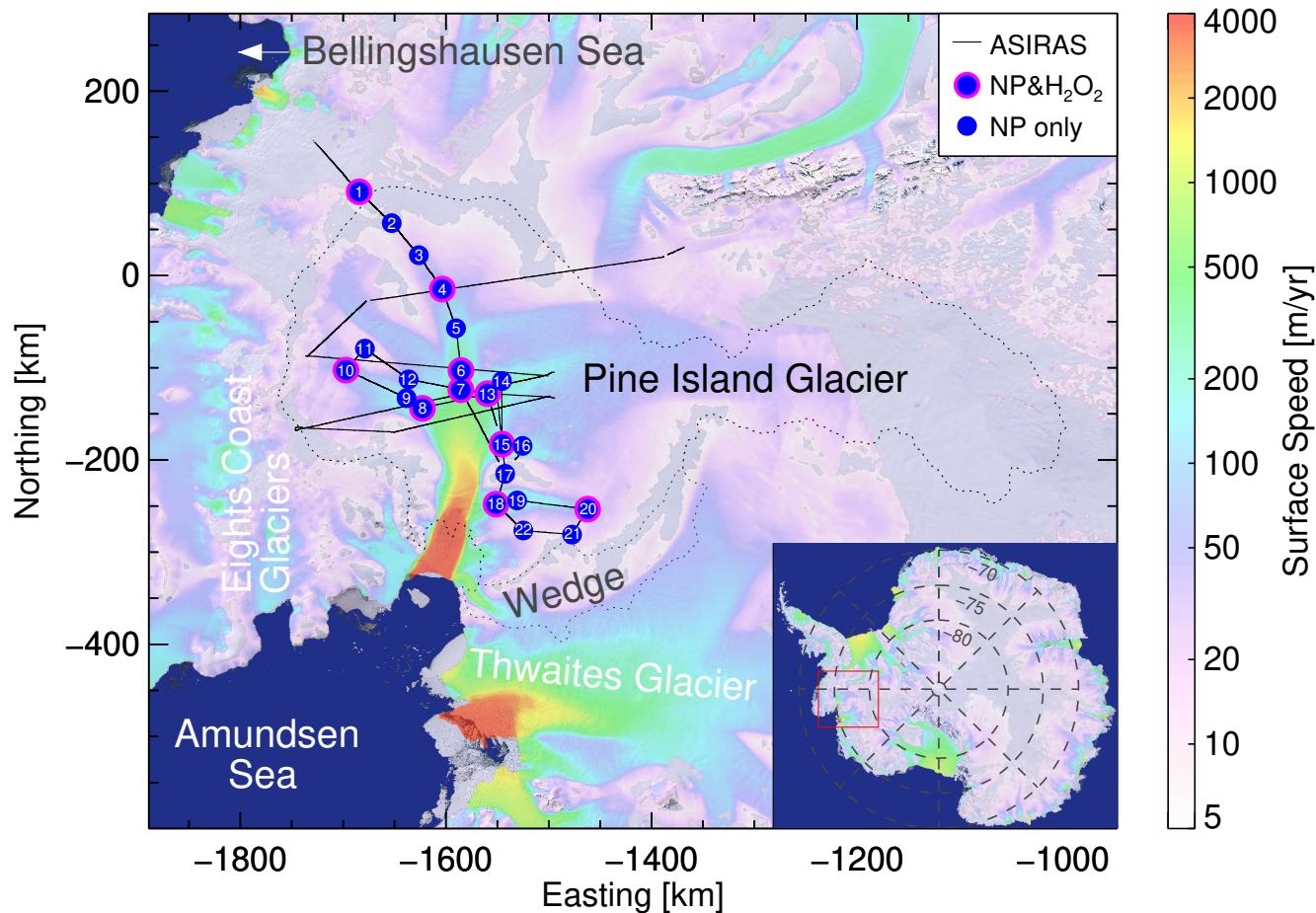
Figure 1. ASIRAS-iSTAR survey projected on polar stereographic coordinates: black lines denote the ASIRAS flight track, numbered blue circles the iSTAR sites with shallow (~ 13 m) neutron probe snow density measurements, and magenta-blue circles iSTAR sites with additional deep (~ 50 m) firn core measurements of H_2O_2 during traverse T2. Surface flow speeds from Rignot et al. (2017) are overlayed by colour shadings on top of Landsat imagery (U.S., Geological Survey, 2007). Dotted lines denote basin outlines based on Fretwell et al. (2013) analysis (data accessed via the SCAR Antarctic Digital Database on 23 April 2019).

2 Data and methods

2.1 iSTAR traverse

The iSTAR traverse followed the PIG main trunk as well as its tributaries as shown in Fig. 1. A total flight track (black lines) of 2486 km was covered by the ASIRAS measurements between 1 and 3 December 2014. Following ME14, the basin outlines (dashed lines) include the Wedge zone between PIG and Thwaites. The main emphasis of the iSTAR campaign was on the fast flowing segments of PIG, thus we lack measurements from the southward interior. Earlier observations from ME14 suggest

radar system	ASIRAS	CReSIS Accu-R	pulseEKKO PRO
vertical range bin (firn)	7.3 ± 0.3 cm	62 cm	100 cm
along track bin	4.5 m	O (10 m)	1.4 m
maximum sampling depth	30 m	300 m	(90-120) m

Table 1. Approximate sample bin resolution and maximum depth of: SAR level_ 1b processed ASIRAS data with indicated vertical range bin standard deviation based on our two-way-travel time (TWT) to depth conversion, CreSIS Accumulation radar according to Medley et al. (2014), and pulseEKKO PRO GPR discussed in Konrad et al. (2019). For the GPR system we estimate the maximum sampling depths based on shared radargrams, which resolve the internal stratigraphy at PIG for TWTs up to (1000-1200) ns.

60   that the SMB decreases towards the interior so the contribution from this area to the total mass input will be less than that from the rest of the basin.

Additional SMB measurements were made with a ground penetrating radar during traverse T1 and published in Konrad et al. (2019). They selected the ~ 1986 reflection layer, which approximately coincides with the observed main reflector by ME14, and traced the layer along sections of the 900 km traverse, amounting to a total of a 613 km distance covered by GPR ob-

65   servations. Due to the limited maximum sampling depth of the ASIRAS and NP measurements, the 1985/86 reflection layer used by ME14 and Konrad et al. (2019) is not contained in most of our data. To benefit from the ASIRAS coverage while simultaneously accounting for its limited depth range, we manually traced the continuous 2005 reflection layer over a distance of 2367 km to derive mean annual SMB estimates for the 2005–2014 period. Due to the reported consistency between the GPR and airborne SMB measurements in Konrad et al. (2019), we limit the comparison of our results to the basin wide estimates by

70   ME14. In addition, we assume that the effect of strain history, which could affect our SMB estimates at the fast flowing sections of PIG, is negligible. Konrad et al. (2019) conclude that the total effect over the whole catchment is small, even though it can have a very significant effect at some sites. However, this effect is expected to be further reduced for the shallower reflection layer depths from the ASIRAS measurements.

2.2 Neutron Probe measurements

75   NP measurements of snow density were performed at all stations during both traverses as described in Morris et al. (2017). To evaluate the effect of densification, they repeated the density profiling in the same boreholes during traverse T2. Because the most recent accumulation is missing in these profiles, they drilled an additional borehole of less than 6 m depth and a nearby distance of about 1 m to capture it during traverse T2. The only exception is site 2, where the ground team decided to auger a completely new 14 m borehole for the density profiling due to poor data from the T1 hole.

80   The deep firn cores (~ 50 m) denoted in Fig. 1 were collected and analysed by the British Antarctic Survey. This analysis includes the annual variations with depth of the photochemical H_2O_2 tracer and density, which are phase shifted by about six months. According to Morris et al. (2017) the annual density variation is caused by alternating late austral summer/autumn low-density hoar layer with winter snow which has densified under the influence of warm summer temperatures. The different
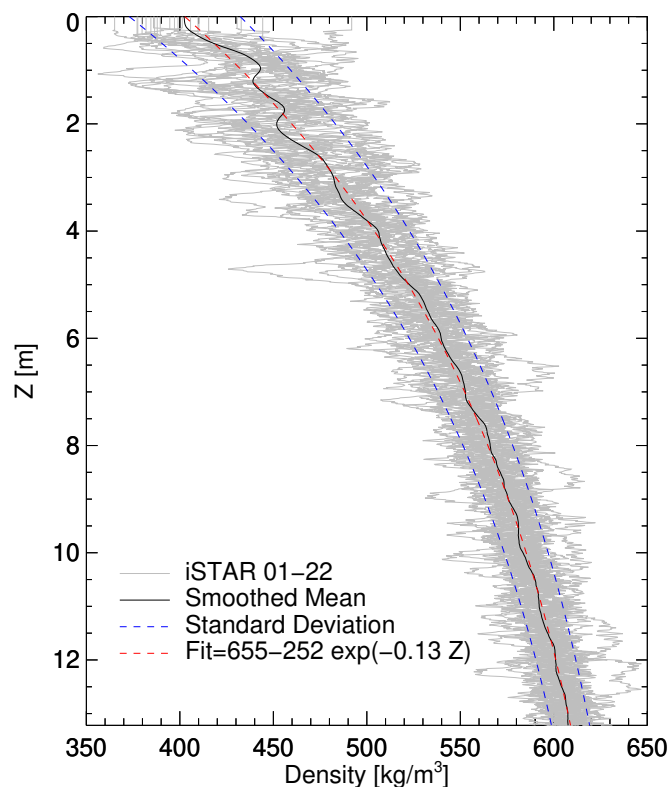
Figure 2. Compiled density–depth profiles from traverse T1 and T2 at all 22 iSTAR sites (grey lines). The black line denotes the smoothed mean profile, the red dashed line an exponential fit (units according to axis annotations), and the blue dashed lines the standard deviation intervals of the fit.

modulating processes of density and H_2O_2 allow for an independent determination of annual snow accumulation at the 10 deep

85 core sites. Morris et al. (2017) applied an automatic annual layer identification routine to their snow density profiles and used the annual H_2O_2 peak depths as an additional guidance for the annual layer dating. Thus, the depth–age scales from both annual markers are consistent.

We use a single regional density–depth profile for the two-way-travel time (TWT) to depth conversion of the ASIRAS soundings, which we derive from the 43 NP profiles of traverse T2. First, we merge the ~ 13 m and nearby ~ 6 m density–depth

90 profiles from the NP measurements during traverse T2 by linearly relaxing their overlapping segments. To reduce the effect of lateral noise convolution, we limit the relaxation length to the overlapping segments that correlate well with each other. Then we align the intercepting depth–age scales to create a consistent depth–age scale for each compiled profile. The resulting merged profiles are shown by the grey lines in Fig. 2. From these profiles, we then determine a smoothed regional mean profile, which is denoted by the black line. Finally we fit an exponential function to the regional mean profile (red dashed line),

95 which we apply to the TWT to depth conversion. The blue dashed lines show the fitted standard deviation of the density as
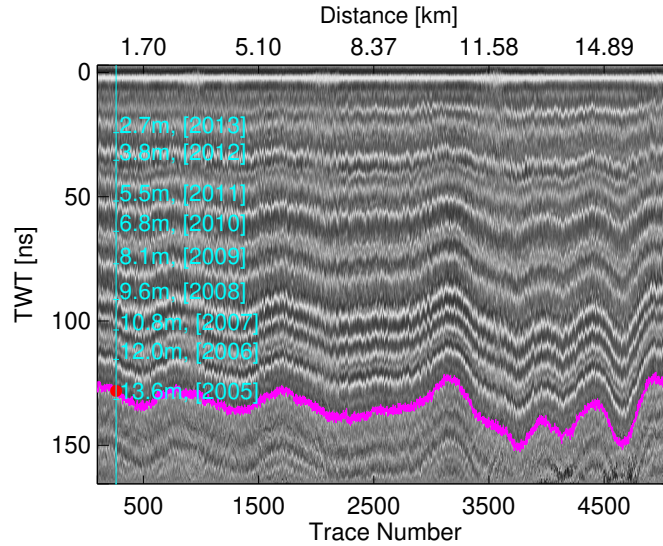
Figure 3. ASIRAS radargram at iSTAR site 21 with surface reflection centred at the origin of the TWT scale: traced layer highlighted in magenta and depth–age scale at point of closest approach highlighted in cyan. The distance and trace numbers refer to the origin of the ASIRAS track segment 20156124 (see Tab. 2).

a function of depth. Following Medley et al. (2013), we consider the fitted standard deviation to be representative for the spatial uncertainty of the regional scale density–depth profile.

2.3 ASIRAS soundings

ASIRAS is a Ku-band radar altimeter which operates at a carrier frequency of 13.5 Ghz and a bandwidth of 1 GHz (Mavro-cordatos et al., 2004). As in a previous campaign in Greenland (Overly et al., 2016), it was operated in Low Altitude Mode at PIG (i.e. less than 1500 m above ground). A Synthetic Aperture Radar (SAR)-processing of the collected data was performed, which yields the spatial resolution of the SAR level_1b data shown in Tab. 1. The associated cross track footprint is ~ 15 m. We use the electromagnetic wave speed $v = c/\sqrt{\epsilon'}$ to convert TWT to depth, where c is the vacuum speed of light and ϵ' is the real part of the dielectric permittivity of the firn column. For the latter, we apply the commonly used empirical relation by Kovacs et al. (1995):

$$\epsilon'_{kov} = (1 + 0.845\rho_s)^2, \tag{1}$$

where $\rho_s = \rho/\rho_w$ is the specific gravity of snow at current depth with regard to the water density $\rho_w = 1000$ kg m^{-3}. An alternative model by Looyenga (1965) is

$$\epsilon'_{loo} = \left(\frac{\rho}{\rho_{ice}} \left[\sqrt[3]{\epsilon'_{ice}} - 1 \right] + 1 \right)^3, \tag{2}$$

110 with $\epsilon'_{ice} = 3.17$ (Evans, 1965) and $\rho_{ice} = 917\,\mathrm{kg\,m}^{-3}$. Sinisalo et al. (2013), who consider a similar depth range to this study, conclude that the difference between wave speeds based on Eq. (1) and (2) has a negligible impact on their SMB estimates. This is also the case for our estimates (see Section 3). The maximum depth of the radargrams is ~ 30 m based on the TWT to depth conversion from the fitted regional mean profile of density with depth and substituted Kovacs relation. The depth range of resolved internal stratigraphy varies along the flight track, but the layering remains visible for most of the upper 13 m

115 depth covered by the NP measurements. Using the mean depth density profile, we determine the w.e. depth value for each waveform bin and calculate the mass per unit area between the selected reflection layer (magenta line in Fig. 3) and surface. We assume that the annual peaks in density lead to reflection layers because of the associated dielectric constant (Eisen et al., 2003). However, we also find that the ASIRAS soundings appear to resolve sub-annual layers at locations where the snow accumulation is high, e.g. around iSTAR site 21 as shown in Fig. 3. These layers may be created by intra-annual events,

120 e.g. hoar events that form thin ice layers (Arcone et al., 2004), which generate a noticeable dielectric contrast with regard to the ASIRAS soundings. Hence, we rely on the independent measurements at the iSTAR sites to distinguish intra-annual from annual layers. Before the layer tracing, we apply an automatic-gain-control filter to all waveforms and limit their dynamic range to twice the standard deviation centred around the mean amplitude of each waveform. This improved the signal contrast of the radargram. Initially we tested a phase following algorithm of the Paradigm EPOS geophysical processing software to trace

125 semi-automatically the selected reflection layer. However, this method became unstable for lower contrast and cases with close layer spacing. Furthermore, remaining SAR-processing artefacts were interfering with the phase following algorithm. Because of the complex nature of the observed stratigraphy, as has been also reported by Konrad et al. (2019), a manual layer tracing was used. Following Richardson et al. (1997), we attempted to bridge distorted or merged layer segments whenever distinct characteristics of a vertical layer sequence could be identified with confidence before and after the bridging. Different processes

130 can lead to distortion of the reflection layers, e.g. processes changing deposition of the annual snow layers or excessive rolling angles of the airplane, while merging layers can result from low snow precipitation and ablative processes (e.g. wind-scouring) or a combination of both. We compared the traced layer at 34 intersections and 8 nearby flight track segments. In case of layer mismatches, the layer tracing was iteratively adjusted to find a consistent layer for the entire flight track. In this sense, the layer tracing is performed independently from the annual layer dating at each iSTAR site.

135 ## 2.4 Measurement error estimation

We attempt to trace the 2005 reflection layer, which is covered by all NP depth–age scales. Following Morris et al. (2017), we define mass balance years between the density peaks in the NP profiles (nominally 1st of July). For instance, the mass balance year 2013 begins at the second annual density peak below the surface (nominally 1st July 2013 and ends at the first peak (1st July 2014). At N points along the closest approach of the ASIRAS track to each iSTAR site we estimated the depth of the

140 reflection layer from its TWT, using the fitted density profile from that site. We also tested the use of the measured density profile for the TWT conversion instead, but we find that the impact on our results is negligible similar to Morris et al. (2017). The estimated depths do not necessarily coincide with the depth of a peak in the density profile i.e with the start of a mass balance year. We assign an estimated date to the mean value of N points by interpolation using the depth–age scale from the

Track Number	iSTAR Site	Year	ΔD [m]	Comment
20156125	1	2003.9 ± 0.2	75	
20156125	2	(2009.88 ± 0.03)	8	erroneous NP dating
20156125	3	2003.39 ± 0.04	11	
20156125	4	2004.9 ± 0.1	86	
20156110	4	2004.5 ± 1	811	
20156125	5	2006.4 ± 0.1	119	
20156125	6	2005.1 ± 0.2	177	
20156106	6	2006.0 ± 0.6	2000	
20156125	7	missing	226	noise
20156115	7	2006.2 ± 0.4	304	
20156113	8	2004.8 ± 0.2	316	
20156109	8	2004.9 ± 0.2	470	
20156113	9	2003.1 ± 0.1	282	
20156113	10	2003.5 ± 0.4	9	
20156114	10	2004.9 ± 0.1	331	
20156114	11	2004.3 ± 0.2	121	
20156115	11	2004.3 ± 0.2	76	
20156115	12	missing	490	noise
20156115	13	2005.5 ± 0.2	127	
20156102	13	2005.7 ± 0.2	56	
20156109	13	2004.7 ± 0.1	377	
20156107	14	2003.5 ± 1	325	
20156109	14	2005.0 ± 0.6	350	
20156107	15	2005.16 ± 0.09	485	
20156120	15	2005.92 ± 0.2	190	
20156107	16	2004.19 ± 0.05	413	
20156103	16	2003.8 ± 0.1	314	
20156120	17	missing	60	noise
20156121	18	2004.33 ± 0.09	186	
20156120	18	(2003.2 ± 0.2)	297	extrapolated
20156126	18	(2002.0 ± 0.4)	867	extrapolated
20156121	19	(1996.8 ± 0.3)	230	extrapolated
20156122	20	2005.12 ± 0.06	15	
20156122	21	2005.73 ± 0.02	115	
20156124	21	2005.71 ± 0.07	26	
20156124	22	2005.65 ± 0.06	21	

Table 2. Dating (Year) with associated uncertainty of closest ASIRAS reflection layer to i^{th} iSTAR site. "Track number" refers to the ASIRAS flight track naming convention and "ΔD" is the closest distance between the ASIRAS track and the iSTAR site. Years in brackets are discarded from the regional layer age estimation for the reasons given in the Comment column.
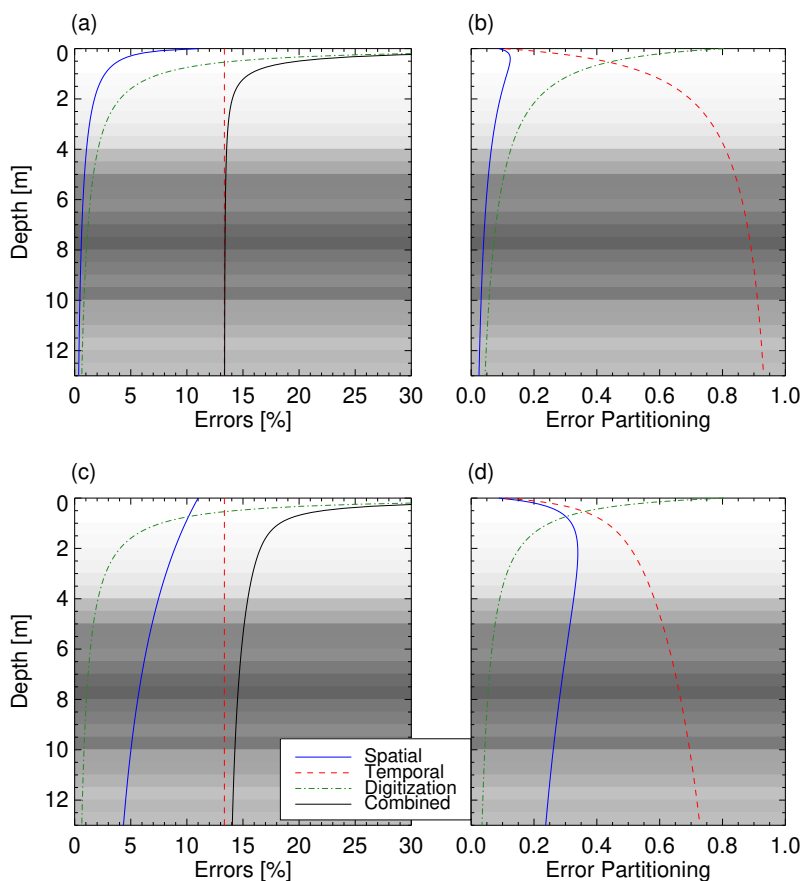
Figure 4. Spatial, temporal, digitization, and combined relative errors (left panels) and error partitioning (right panels). Grey background shades indicate the depth distribution of the traced 2005 reflection layer. (a,b) Based on error propagation according to Eq.(5). (c,d) Excluded error cancellation for the spatial error terms (see text).

iSTAR site. These points are centred around the point of closest approach to the nearby iSTAR GPS location. We chose the
associated interval length to be twice the distance ΔD between the iSTAR GPS location and point of closest approach of the
flight track. Finally, we added six months to the estimated dates according to the mass balance year definition. This yields the
estimated Year values for the reflection layer at each iSTAR site in Tab. 2. Following Konrad et al. (2019) we express the dating
uncertainty as the standard deviation σ_x in the N measurements. In this sense, our error estimate is more conservative than the
standard error of the mean. Furthermore, we assume that the uncertainty due to local variation in the stratigraphy is isotropic,
which does not generally need to be true. However, according to Tab. 2 in most cases the overall impact of this effect is one
order of magnitude smaller than the variability of dated years among all iSTAR sites. As indicated in Tab. 2, we excluded dating
estimates around iSTAR sites 2 and 19. In both cases, our layer tracing revealed a large offset contrary to the neighbouring
iSTAR sites. Possible reasons for these offsets could be systematic errors in the layer dating from the NP profiles, the variability

of internal stratigraphy between the ASIRAS measurements and their closest approach to both iSTAR sites or systematic errors

in the manual reflection layer tracing. The remaining exclusion of dating estimates at iSTAR sites 7, 12, and 18 is either due to

high noise levels of the radargram or reflection layer depths exceeding the NP depth–age scales. Following Konrad et al. (2019)

we estimate the reflection layer year by the mean of dating values at each site with an uncertainty of $\Delta t = \sqrt{\overline{\delta t}^2 + \delta \overline{t}^2 + \overline{t}_x^2}$,

with the annual layer tracing uncertainty $\overline{\delta t} = \pm 1$ years, the standard deviation of dating estimates $\delta \overline{t}$, and the propagated error

$\overline{t}_x = 1/n \sqrt{\sum_i^n \sigma_x(i)^2}$ from the n lateral error estimates around each iSTAR site (i = site number), which we introduced in

addition. The resulting reflection layer dating estimate is $T = 2004.8 \pm 1.4$, which corresponds to a layer age of $a = 10.1 \pm 1.4$.

The associated average surface accumulation rate $\dot{b}$ in terms of w.e. depth per year is

$$\dot{b} = \frac{1}{a\rho_w} \sum_{i=1}^{m} \delta z_i \rho_i, \tag{3}$$

where δz_i is the ith depth increment of the radar waveform and ρ_i is the associated density. Substitution of the wave propagation

speed for δz_i yields

$$\dot{b} = \frac{1}{a\rho_w} \sum_{i=1}^{m} \frac{ct_s}{\sqrt{\epsilon'_i}} \rho_i, \tag{4}$$

where $t_s = 0.37$ ns is the ASIRAS vertical bin sampling time (i.e. $0.5 \times$ TWT per bin), and ϵ'_i refers to the permittivity value

at the ith bin. To avoid any confusion with previous summations, the final index m refers to the traced waveform bin at the

reflection layer depth. It is evident from Eq. (4) that the spatial uncertainty of the density profile affects both the integration

depth and incremental mass. Medley et al. (2013) and ME14 estimated the spatial uncertainty from the resulting SMB change

by directly applying the standard deviation fits of their regional density profiles to the TWT to SMB conversion. Instead, we

may propagate the error in Eq. (4), assuming that errors are uncorrelated and normally distributed. Based on the Kovacs relation

according to Eq. (1) we account for the temporal, spatial, and digitization:

$$\Delta \dot{b} = \frac{ct_s}{a\rho_w} \sqrt{\underbrace{\sum_{i=1}^{m} \left(\frac{\Delta\rho_i}{\epsilon'_{kov,i}} \right)^2}_{\text{spatial}} + \underbrace{\left(\frac{\Delta a}{a} \sum_{j=1}^{m} \frac{\rho_j}{\sqrt{\epsilon'_{kov,j}}} \right)^2}_{\text{temporal}} + \underbrace{\left(\frac{1}{3} \cdot \sum_{k=m-1}^{m+1} \frac{\rho_k}{\sqrt{\epsilon'_{kov,k}}} \right)^2}_{\text{digitization}}}, \tag{5}$$

where $\Delta a = \pm 1.4$ years is the temporal uncertainty and $\Delta \rho_i$ are the standard deviation intervals according to Fig. 2. Due to the

small incremental density change of $< 0.7\%$ along the entire profile, we approximate the digitization error by the mean SMB

value of three consecutive bins centred at the final profile bin of the current integration depth. Figure 4 (a) displays the integrated

individual measurement error components as well as the combined error according to Eq. (5) as a function of geometric depth.

In addition, we include the error partitioning in (b). The grey background shades highlight the distribution of layer depths to

visualise the relevant error range of our SMB estimates, which peaks around (5, 8, and 10) m. By comparison with Medley

et al. (2013) and ME14, we find that our spatial error estimate based on Eq. (5) is reduced by about one order of magnitude

while the standard deviation fits of their regional density profiles cover a similar range compared to ours. We may ignore the

spatial error compensation in Eq. (5) by replacing the root-sum-of-squares (RSS) with absolute values: $\sum_{i=1}^{m} \left(\Delta\rho_i/\epsilon'_{kov,i} \right)^2 \rightarrow$

$\left(\sum_{i=1}^{m} |\Delta\rho_i/\epsilon'_{kov,i}| \right)^2$. Hence, to comply with the studies above, we consider the more conservative spatial error propagation
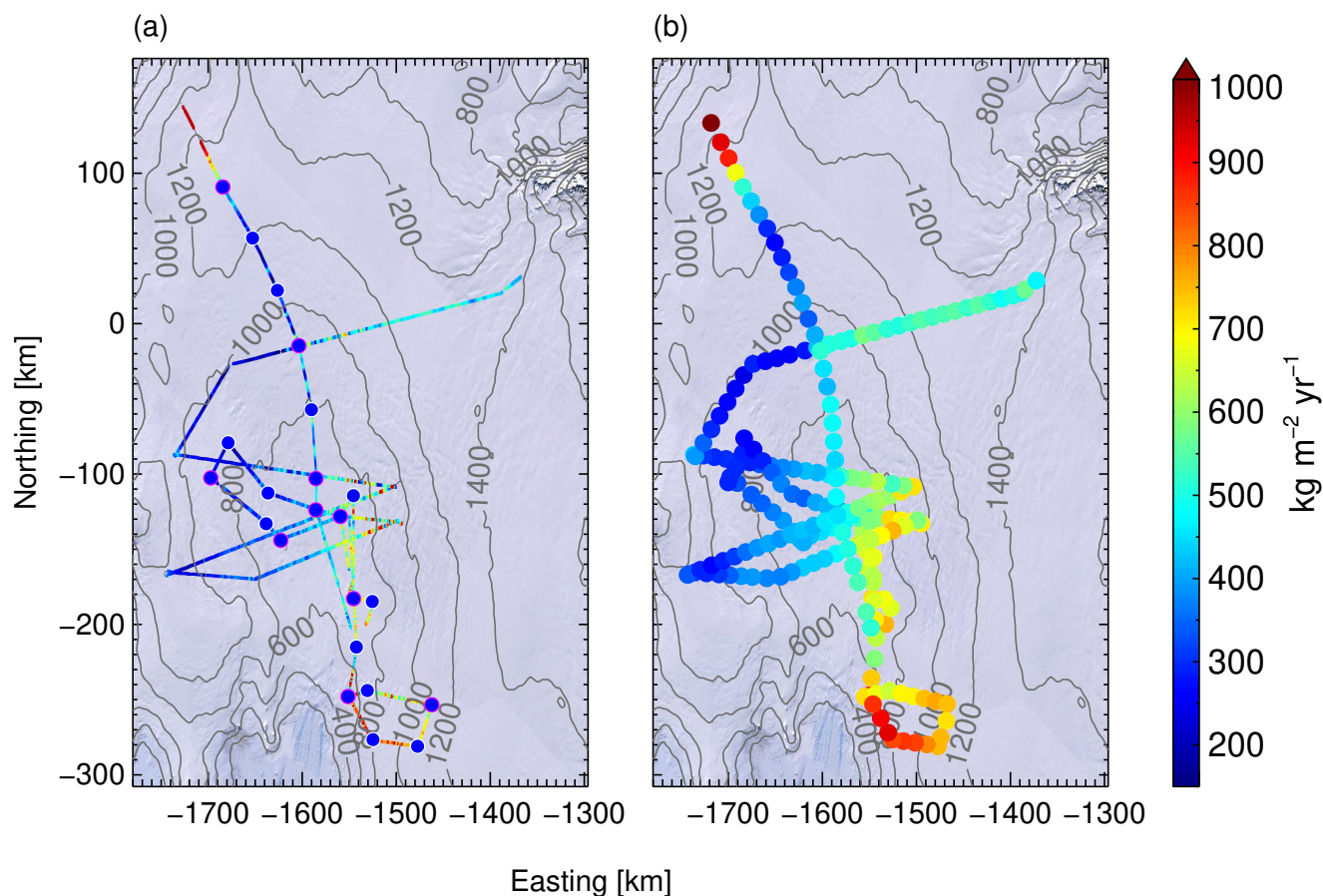
Figure 5. Traced annual mean SMB between November 2004 and December 2014 from ASIRAS soundings with overlayed contour lines from a digital elevation model (see text) and landsat background imagery (U.S., Geological Survey, 2007). (a) High spatial resolution, iSTAR sites denoted by magenta/blue circles (deep cores) and white/blue circles (shallow cores). (b) Smoothed and downsampled SMB estimates as described in the text.

based on the sum of absolute values, but we keep the RSS of individual error components for the combined measurement error
185 estimate as shown in Fig. 4 (c-d). Following these assumptions, we find that our measurement error estimate is still dominated by the temporal layer dating uncertainty for most of the traced layer depths, but the spatial error reaches a similar range as reported in Medley et al. (2013).

2.5 Kriging scheme

We focus on the regional scale variability of the SMB distribution on PIG. Figure 5 shows our high resolution (i.e. metre-scale)
190 SMB estimates as well as smoothed SMB values with contour lines from a digital elevation model (DEM) by Helm et al. (2014). We use the same 25 km along-track smoothing window as ME14 and choose a sampling interval of half the smoothing
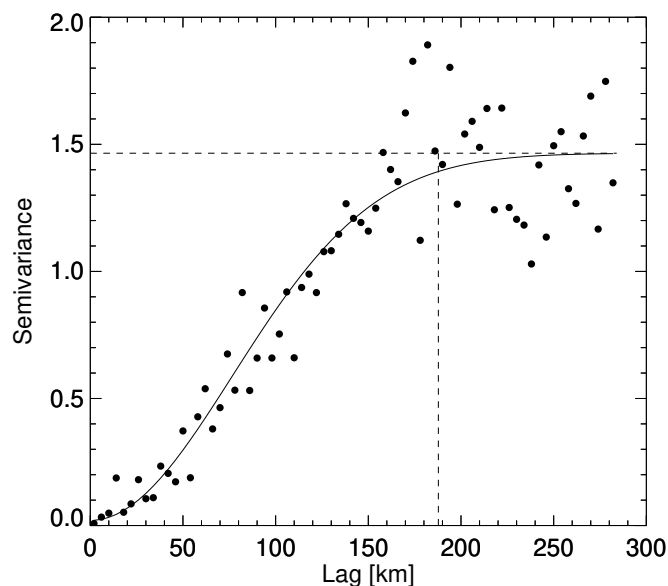
Figure 6. Experimental semivariogram of log-transformed smoothed SMB observations (dots), Gaussian fit model (black solid line), sill and practical range parameter (dashed lines).
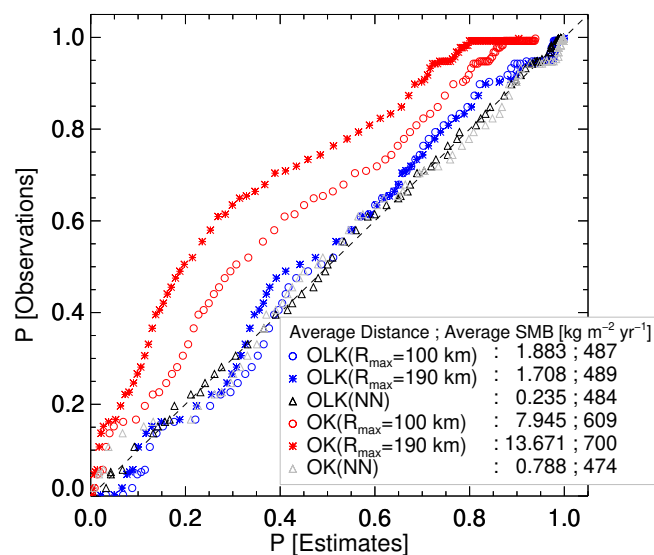
Figure 7. PP-plots between SMB observations and estimates based on OK and OLK interpolation methods for varying maximum estimate distances with regard to the closest measurement locations. The dashed 1:1 line indicates the complete PP-agreement between observations and estimates. Average PP-distances (see text) and SMB values are shown in the figure.

window length. We initially tested the same interpolation scheme as described in ME14 to estimate a regional scale SMB field for the PIG basin from our smoothed SMB points. This scheme is based on the ordinary kriging (OK) algorithm, a widely used

geostatistical interpolation technique (e.g. Isaaks and Srivastava, 1991). Instead of a direct OK interpolation of smoothed SMB
195 observations, ME14 consider the residual SMB values with regard to an ordinary least squares linear regression model for the
Thwaites-PIG basin area with northing, easting, and elevation as explanatory variables. This, in turn, yields a small degree of
skewness < 0.5 of their new SMB distribution. However, we failed to reduce the skewness of residual SMB values effectively
by the same method, which may by due to the different aerial coverage considered in our regression model. Examination of the
DEM contour lines in Fig. 5 reveals that a simple relation between surface elevation and SMB is not evident, which may hint
200 that the prevailing synoptic scale weather conditions at the Amundsen and Bellingshausen Sea sectors in combination with the
precipitation shadowing effect of the Eights Coast mountain range (Fig. 1) require a more sophisticated model to capture the
SMB at the PIG basin scale. An alternative approach, which is also mentioned in ME14, is a logarithmic transformation of the
SMB observations prior to the OK interpolation:

$$\dot{B}(x_0) = \ln\left(\dot{b}(x_0) + C\right), \tag{6}$$

205 where C is an arbitrary constant and x_0 represents the current interpolation location. After the OK interpolation of transformed
SMB observations, the estimates must be transformed back into the original measurement scale. This backtransformation
requires the addition of a nonbias term for each OK estimate to ensure that the expected value is equal to the sample mean and
that the smoothing effect is adequately compensated (i.e. resulting estimates reproduce the sample histogram and sample mean
[Yamamoto, 2007]). We implemented such ordinary logarithmic kriging (OLK) method in our analysis by adopting the 4-step
210 post-processing algorithm proposed by Yamamoto (2007) for the estimation of nonbias terms. According to Yamamoto (2008),
OLK does not necessarily require a log-normal sample distribution to produce improved estimates in terms of local accuracy.
Furthermore, Yamamoto (2007) tested the impact of constant C according to Eq. (6) and found that a data translation towards
higher values yields an approximation from OLK to OK estimates, thus, eliminating the advantage of improved sample mean
reproduction and local accuracy of OLK estimates. Indeed, we find that adding a negative constant C to all SMB values, such
215 that the lowest SMB value reaches $0.1 \, \mathrm{kg \, m^{-2} yr^{-1}}$, yields an improved reproduction of the observation data characteristics.
Figure 6 shows the experimental isotropic semivariogram of our log-transformed SMB observations from Fig. 5 (b) together
with a Gaussian model fit with a practical range of $\sim 190 \, \mathrm{km}$, i.e. the range at which the spatial autocorrelation of sample points
is vanishing. Following Yamamoto (2005, 2007), we investigate the reproduction of observational data characteristics by means
of PP-plots (i.e. percentiles of cumulative distributions of observations and estimates against each other). Figure 7 shows the
220 PP-plots for our OLK and OK interpolation constrained to a maximum estimation range with regard to the closest ASIRAS
measurement locations of (100 and 190) km, and nearest neighbour locations. By comparison with Fig. 6, the (100 and 190) km
distances (dashed lines) approximately correspond to the lag distances at which the semivariogram has reached half the sill and
where it has levelled off respectively. In addition, the average distance of PP-points from the 1:1 line according to the definition
in Yamamoto (2005) as well as the average SMB values for the OK and OLK estimates are shown in the legend. Both, the
225 nearest neighbour OK and OLK average SMB estimates are close to the average SMB observation value of $474 \, \mathrm{kg \, m^{-2} yr^{-1}}$.
However, after extending the estimation range, it is evident from Fig. 7 that the best match exists between the observation and
OLK estimation values. Hence, we limit our analysis to these values in the following.

Aside from the choice of the translational constant C and semivariogram model, we choose the proposed method by Deutsch (1996) to correct for negative kriging weights (Yamamoto, 2000) and constrain all processing steps of the OLK estimation to

230   the 16 nearest neighbours for each estimate according to the quadrant criterion. Depending on the considered neighbourhood the effect of smoothing as well as local stationarity of observation data is affected. As a guidance for our final setting, we aimed at generating an optimal PP-relation according to Fig. 7, but also considered potential artefacts, which may arise from the OLK procedure.

In addition to each OLK estimate, we calculate the associated interpolation error. While ME14 choose the kriging standard

235   deviation as a measure of interpolation error, our error estimation is based on the introduced interpolation standard deviation S_0 by Yamamoto (2000) for two reasons. Firstly, as shown by the author, S_0 represents a more complete measure of local accuracy and has, therefore, been implemented in the post-processing algorithm in Yamamoto (2007). Secondly, for the OLK method we need a corresponding backtransformation of the interpolation error from the logarithmic to the measurement scale, which has already been investigated for S_0 in Yamamoto (2008). Thus, we adopted the proposed backtransformation of S_0 in

240   this study.

Following ME14, we estimate the total error of each SMB estimate by the RSS of the measurement error and transform S_0 back. The measurement error is estimated by generating 500 realisations of OLK SMB estimates with add noise to the smoothed SMB observations, which follows a normal distribution with a mean of zero and standard deviation equal to the measurement error of the SMB observation at x_0.

245   For the basin wide SMB estimation we have to keep in mind that our OLK estimation is limited in terms of the practical range according to Fig. 6. By comparison with the flight track shown in Fig. 1, even when considering the practical range as a maximum threshold for the spatial SMB estimation, we do not cover the entire PIG basin. Hence, for the calculation of total mass input for the PIG basin, we replace our SMB estimates with modelled SMB from the RACMO2.3p2 (van Wessem et al., 2018) regional climate model(in the following abbreviated as RACMO) at distances where the spatial autocorrelation of

250   measurements is low.

3   Results

3.1   Regional scale SMB distribution

Based on the adopted OLK interpolation scheme, we produced the mean annual SMB map for the PIG basin from the ASIRAS observations in Fig. 8 (a). SMB observations and estimates are colour coded with the same scale. Each estimate covers a pixel

255   size of ~ 5 by $5~\mathrm{km}^2$ and refers to the averaging period between November 2004 and December 2014. The two surrounding dashed lines indicate the (100 and 190) km maximum distances from the ASIRAS measurement point cloud as discussed earlier. The red triangle denotes an artificial interpolation cluster of 8 pixels with SMB values greater than $2000~\mathrm{kg\,m^{-2}yr^{-1}}$, which we will discuss in Sec. 4.3.

By comparison with ME14 and the extracted RACMO estimates in Fig. 8 (b), the regional SMB distribution at PIG reproduces

260   the same main characteristics, i.e. increasing SMB rates towards the Amundsen Sea coastline, decreasing SMB rates towards
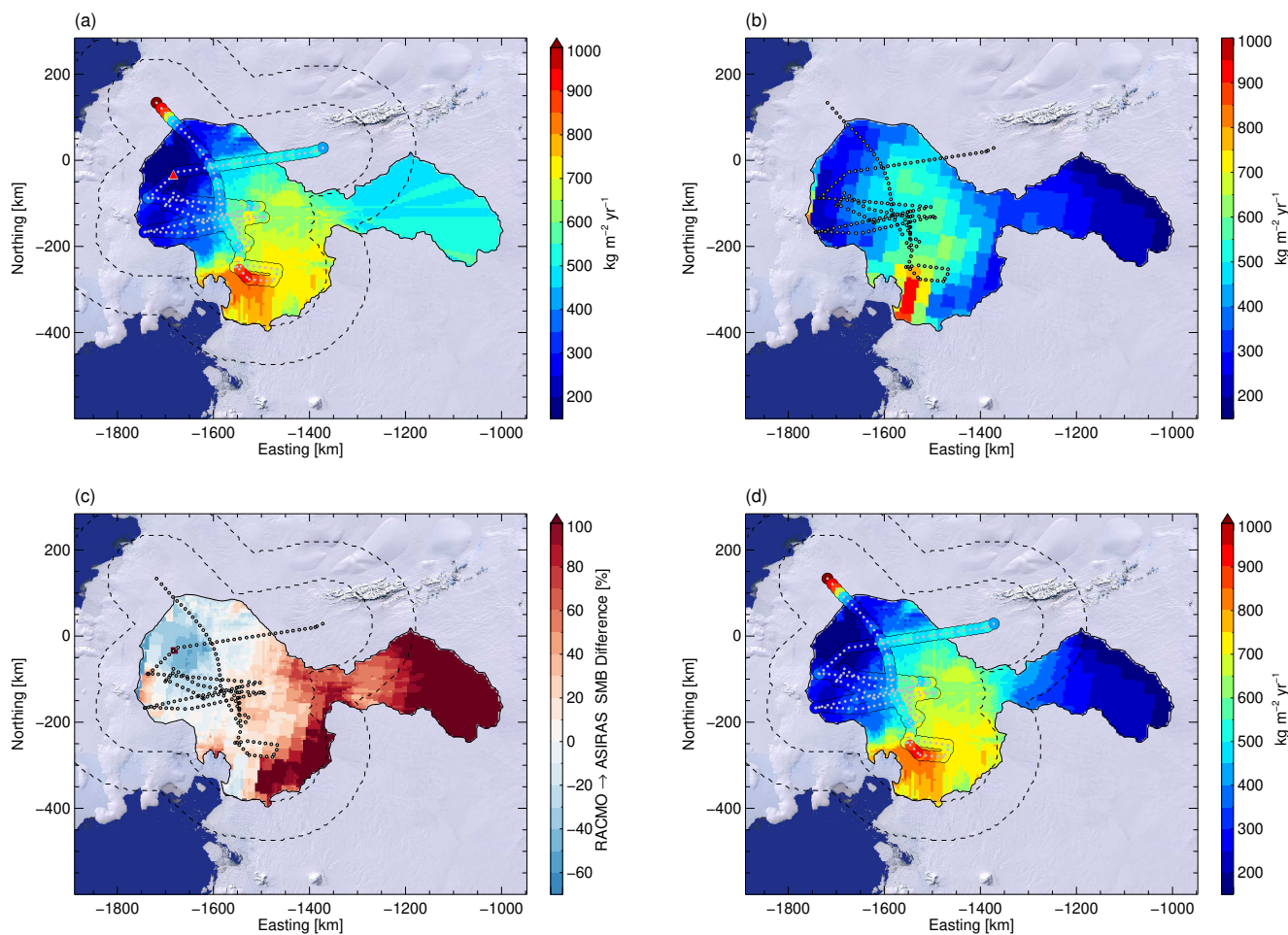
Figure 8. (a) ASIRAS annual mean SMB OLK estimates between November 2004 and December 2014. Measurement points colour coded with the same SMB scale. Red triangle denotes the position of an interpolation artefact (see Sec. 4.3). (b) RACMO annual mean SMB estimates for the same averaging period as in (a). ASIRAS measurement locations denoted by dots. (c) Relative SMB change from RACMO to ASIRAS, i.e. $[(a) - (b)]/(b) \times 100$. (d) Hybrid SMB map with (a) linearly relaxing into (b) between dashed lines (a,c,d), which denote the (100 and 190) km maximum distance to the ASIRAS measurements. Background imagery taken from U.S., Geological Survey (2007) for all panels.

the inland, and a region of low SMB in response to the shadowing effect from the Eights Coast mountain range. The RACMO estimates indicate a sharp boundary of this effect at the ice divide at the northern tip of PIG. This boundary is also captured by the ASIRAS observations at its northernmost flight track near iSTAR site 10, which is best seen in the high resolution observations according to Fig. 5 (a).

265 Fig. 8 (c) shows the relative difference between RACMO and ASIRAS estimates as defined in the caption. It is evident that the shadowing effect is more pronounced in the ASIRAS observations, while the southward SMB gradient is more pronounced in
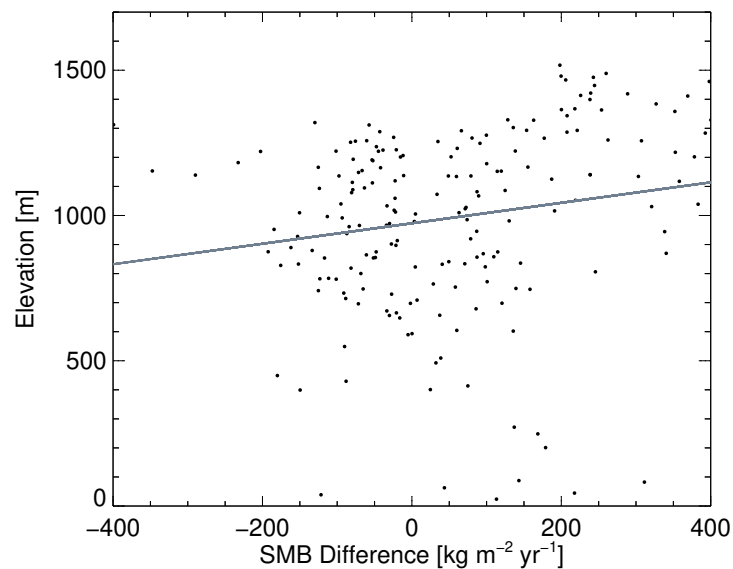
Figure 9. ASIRAS "minus" RACMO SMB estimates as a function of elevation based on Helm et al. (2014) with linear regression line.

the RACMO estimates. Despite the missing ASIRAS observation towards the southern interior, the latter is already apparent inside the 100 km maximum distance margin (inner dashed line). By comparison with the SMB distribution according to ME14, we find similar departures to our results with respect to the northern slopes of PIG and its southward interior.

270 The ME14 results indicate an elevation dependent drift between observed and simulated SMB values, which we also find between our results and RACMO as shown in Fig. 9. Here, we first calculated the average SMB for each RACMO pixel from collocated ASIRAS estimates. Then we subtracted the RACMO SMB estimates from the ASIRAS averages and plot the resulting difference against their associated elevation, which we determined from the DEM model in Fig. 5. Due to the limited practical range of the ASIRAS observations, we only consider ASIRAS–RACMO estimates within the 100 km maximum range

275 limit to the observations inside the PIG outlines. Like ME14, we find for this version of RACMO that simulated SMB estimates appear to be lower than the ASIRAS estimates at higher elevation levels and vice versa. Despite the scatter between elevation and SMB difference, a Kendall's rank correlation test with $\alpha = 0.05$ significance level suggests that both are significantly correlated with each other.

3.2 Total mass input

280 For the calculation of spatially integrated SMB, denoted by Σ_+ in the following, we produced the hybrid SMB map in Fig. 8 (d), where the ASIRAS SMB estimates are linearly relaxed into the RACMO SMB estimates between the 100 km and 190 km range limits to account for the spatial autocorrelation in terms of Fig.6. Table 3 summarizes Σ_+ and further statistical SMB characteristics for different data sets and basin definitions according to Fig. 10 (d). Here, we replaced the interpolation artefact highlighted in Fig. 8 (a) with averaged values from neighbouring pixels. Σ_+ uncertainty estimates refer to the RSS of the

Data Set	Basin	Gt yr^{-1}	kg m^{-2}yr^{-1}				%	
		Σ_+	μ_b	σ_b	min	max	OLK Area	OLK Σ_+
	Pine Island	69.0 ± 17.6	421	195	147	958	72.1	82.9
	Wedge	10.9 ± 1.6	729	48	591	847	99.5	99.6
Hybrid	Pine Island and Wedge	79.9 ± 19.2	447	206	147	958	74.4	85.2
	PIG (Mouginot et al., 2017)	77.5 ± 19.2	439	198	132	958	75.3	85.1
	PIG (Zwally et al., 2012)	92.4 ± 22.4	443	195	79	958	74.6	84.0
	Pine Island	64.7 (65.8)	395 (401)	147 (152)	147 (144)	935 (989)		
	Wedge	6.6 (7.1)	439 (476)	180 (189)	287 (315)	935 (989)		
RACMO	Pine Island and Wedge	71.2 (72.9)	398 (408)	151 (157)	147 (144)	935 (989)		
	PIG (Mouginot et al., 2017)	70.6 (72.1)	400 (409)	150 (157)	132 (131)	935 (989)		
	PIG (Zwally et al., 2012)	81.6 (83.6)	392 (401)	151 (158)	0 (0)	935 (1005)		
Medley et al. (2014)	Pine Island	67.3 ± 6.1	400	130	210	840		
	Wedge	11.0 ± 0.7	590	160	160	330		

Table 3. Spatially integrated SMB (Σ_+), mean (μ_b), standard deviation (σ_b), minimum, and maximum SMB based on different data sets and basin definitions according to Fig. 10 (d). For the hybrid SMB estimates of this study, the areal contribution as well as the contribution of spatially integrated SMB from the ASIRAS estimates is denoted by OLK Area and OLK Σ_+ respectability. In addition to the November 2004 to December 2014 averaging period of the hybrid estimates, RACMO estimates in brackets refer to the July 1985 to January 2010 averaging period in accordance with the results from Medley et al. (2014).

285 interpolation and measurement error-grids (Fig. 10 d) in accordance with ME14. Because RACMO is missing an error-grid, we consider the total combined error for the entire PIG basin as a conservative error estimate. In this sense, we are augmenting the missing model error estimation. To quantify the relative contribution of ASIRAS to the hybrid SMB estimates, OLK area and OLK Σ_+ denote the relative contribution in terms of covered land area and integrated SMB respectively. For comparison with our hybrid based estimates, we include results from RACMO and ME14, which we converted from w.e. depth to SI units.

290 Because of the different averaging periods between this study and ME14, we add RACMO estimates in brackets, which we extracted based on the same averaging period as the ME14 results.

Pine Island and Wedge Zone

The Pine Island Σ_+ values are in agreement between all data sets within the estimated error margins. This is different for the Wedge outlines, where the RACMO Σ_+ estimates are between 35-40) % lower compared to the estimates of this study and

295 ME14. Increasing the averaging time of RACMO estimates to the 1985–2009/10 period of the ME14 results yields an increase of Σ_+ by 2% for the Pine Island and 8% for the Wedge outlines. In comparison with the ASIRAS and ME14 estimates, the simulated total mass input for the Wedge outlines remains outside the error margins of both observations. Considering the further SMB properties according to Tab. 3, the hybrid SMB estimates show the largest variability and range for the Pine

Island outlines. This is different for the Wedge outlines, where the hybrid SMB estimates appear to be larger for most of the
300 basin area.

Additional basin definitions

Tab. 3 includes results based on two additional basin definitions for PIG. Figure 10 (d) shows a composite plot of all basin
definitions used here. The surface areas range between 176.5, 178.6, and 208.8×10^3 km^2 for the PIG basin (including Wedge)
according to the definitions of Mouginot et al. (2017), Fretwell et al. (2013), and Zwally et al. (2012). Alongside with extended
305 surface cover according to Zwally et al. (2012), Σ_+ estimates increase between 16 to 19 % with regard to the other basin
definitions. The impact on the mean annual SMB is limited to 10 kg m^{-2}yr^{-1} ($\sim 2\%$) between all catchment definitions.

4 Discussion

We discuss first the pronounced differences between annual layer dating from ASIRAS reflection and neutron probe density
profiles at some sites and then secondly the systematic differences in SMB distribution between our results and those of ME14
310 and RACMO.

4.1 SMB departures

Key to the evaluation of our selected internal reflection layer is its isochronic nature, which we assume based on matched
depth–age relations from the iSTAR ground truthing measurements. One may argue that these measurements can be subject to
local noise in the density profile, which would challenge any comparison with nearby radar observations. For instance, Laepple
315 et al. (2016) observed dominating stratigraphic noise at single pit density profiles near Kohnen station (East Antarctic plateau,
Dronning Maud Land). Stacking of multiple profiles is one possibility to filter out noise. While this is not possible for the
single iSTAR sites, the estimated dating uncertainty of ± 1.4 years according to this study suggests that iSTAR ground truthing
measurements at PIG are less prone to stratigraphic noise, which is most likely to be related to the higher SMB compared to
~ 70 kg m^{-2}yr^{-1} nearby Kohnen station (Laepple et al., 2016). However, on a few occasions we identified larger departures
320 in the annual layer dating, as it is the case for iSTAR site 2 (Tab. 2). While the layer tracing appears to be in agreement
between site 1 and 3, the annual layer dating at site 2 would suggest an SMB of ~ 290 kg m^{-2}yr^{-1} at the traced layer cross
section rather than ~ 150 kg m^{-2}yr^{-1} based on the 2004.8 layer dating of this study. Accordingly, local SMB results would
increase by $\sim 100\%$, if we used the uncorrected depth–age scale at site 2, which most likely indicates a systematic error in the
measurement scale. This is further corroborated by the measured SMB of 140 kg m^{-2}yr^{-1} at site 2 for the most recent 2014
325 layer, but also measured density and strainrate profiles suggest a mean annual SMB of 200 kg m^{-2}yr^{-1} based on theoretical
grounds, which both are in a better agreement with the collocated ASIRAS based results. In this sense, the ASIRAS results
allow us to be more confident of the site 2 strainrate measurements and therefore add to the densification analysis of Morris
et al. (2017). The local SMB estimates near site 2 from ME14 and RACMO are within the 200 to 300 kg m^{-2}yr^{-1} range, but
lack the local precision of ASIRAS measurements and therefore could not explain the measured density and strainrate profiles

Study	Period	Basin Definition	Σ_+^- ($\mathrm{Gt\,yr^{-1}}$)	Updated Σ_+^- ($\mathrm{Gt\,yr^{-1}}$)
Medley et al. (2014)	2005 - 2012	Pine Island (Medley et al., 2014)	-41 ± 7	-39 ± 18
Medley et al. (2014)	2005 - 2010	Wedge (Medley et al., 2014)	-0.6 ± 2.5	-0.7 ± 3.1
Gardner et al. (2018)	2008 - 2015	Zwally et al. (2012)	-49 ± 19	-40 ± 28
Rignot et al. (2019)	2005 - 2014	Mouginot et al. (2017)	-51 ± 7	-46 ± 20

Table 4. Updated mass balance estimates Σ_+^- for different studies based on hybrid Σ_+ estimates of this study. Indicated periods refer to the considered ice loss processes. Net gain from Σ_+ is assumed to be stationary during the indicated periods.

330 at site 2.

Nearby ASIRAS observations at site 18 and 19 in particular suggest higher SMB values compared to the dated NP profiles. Site 19 is directly located at the centre of a pronounced accumulation trough of $\sim 2.5\,\mathrm{km}$ width, which adds to the uncertainty in the layer matching because of the spatial displacement between the iSTAR site and point of closest approach. Because the traced reflection layer exceeds the depth range of the NP density profiles at site 18 and 19, we discarded both sites for the layer

335 dating.

Additional local departures between our results and those from ME14 were identified for the northern slopes and southward interior of PIG. Because of difficulties in the layer tracing at the northern slopes, they had to augment their SMB estimates with results from a diferent layer, which they dated back to 2002 and corrected for a temporal bias to the 1985 layer based on overlapping segments. Thus, one possible explanation for the observed differences is that the true local temporal bias

340 correction may be different from the regional scale bias correction, which they estimate from regression models. Other possible explanations are differences in the observational coverage and local accuracy from the different interpolation methods. With regard to the southward interior, the spatial coverage is superior for the ME14 results. Despite our limit of a maximum range between $100\,\mathrm{km}$ and $190\,\mathrm{km}$ for the ASIRAS based estimates, the missing observational constraints towards the interior may still yield an underestimation of the southward SMB gradient. However, we also cannot rule out that the smaller gradient in

345 our observations is due to a local increase in SMB between the different observational periods among both studies. Additional observational constraints of the selected reflection layer may resolve the cause on the observed difference.

4.2 Impact on recent mass balance estimates

Despite the local differences in the SMB distribution, the difference between the Σ_+ estimates for the PIG catchment (including Wedge) between this study and ME14 is small, i.e. our Σ_+ is greater by $1.7\,\mathrm{Gt\,yr^{-1}}$, which corresponds to 2% of

350 the ME14 value. This indicates that the local differences in the SMB estimates between both studies cancel out. If we take into account that the temporal averaging time used by ME14 is about a factor of 2.7 larger than that used in this study, this indicates that the observed total mass input for the PIG basin is not subject to any secular trend throughout the observational period, a finding which is further corroborated by the iSTAR measurements and RACMO simulations. This provides additional evidence to Medley et al. (2013) that the recent temporal evolution of the PIG mass balance is primarily driven by dynamic ice

%	Pine Island				Wedge			
	μ_{err}	σ_{err}	min	max	μ_{err}	σ_{err}	min	max
Measurement Error	9.9 (7.2)	5.2 (1.8)	3.7	40.5	7.2	0.9	5.8	9.5
S_0	32.2 (25.5)	32.7 (34.9)	0.5	481.8	12.5	11.3	2.1	57.3
Combined Error	34.4 (27.4)	32.4 (34.2)	6	481.9	15.2	10.2	7.3	57.8
Medley et al. (2014)	10.4	6.1	2.6	30.0	6.3	1.8	2.9	10.8

Table 5. Mean μ_{err}, standard deviation σ_{err}, minimum, and maximum gridded SMB errors. Mean and σ values in brackets refer to the catchment area within the 190 km practical range limit and are weighted in terms of the ASIRAS partitioning of the final hybrid SMB map in Fig. 8 (d).

355 loss into the Amundsen Sea.

With regard to existing mass balance estimates for PIG, we have to take into account that the definition of basin can differ significantly as illustrated in Fig. 10 (d). To evaluate the impact of our hybrid SMB estimates on recent mass balance inventories, we extracted results from the literature in Tab. 4 and added updated mass balance estimates Σ_+^- by replacing the Σ_+ estimates from the literature with the Σ_+ estimates of this study. For the periods shown, we assume that the SMB remains stationary for

360 the mass balance calculation. In addition, we linearly interpolated the estimated ice discharge measurements in ME14 for the missing periods before 2007. Furthermore, we assume that the unspecified basin definitions in ME14 are in close agreement with the basin definitions based on Fretwell et al. (2013).

The small difference between the Σ_+ estimates of this study and ME14 directly translates into the Σ_+^- mass balance estimates. The largest impact of our results is on the Σ_+^- estimate by Gardner et al. (2018). After replacing their Σ_+ estimate from

365 RACMO2.3 simulations with our hybrid Σ_+ estimate, the mass balance increases by $\sim 9\,\mathrm{Gt\,yr^{-1}}$.

4.3 SMB uncertainty

While the agreement in Σ_+ estimates between this study and ME14 supports the hypothesis that the regional SMB of PIG is stationary at decadal scales, our uncertainty estimates are much larger. The temporal error according to Fig. 4, which is $\sim 5\%$ larger than Medley et al. (2013) and ME14, cannot fully explain the difference between both uncertainty estimates. We also

370 do not expect any major differences with regard to the spatial uncertainty of the density profiles. According to the error-grid statistics in Tab. 5, we identify the backtransformed interpolation standard deviation S_0 from the OLK scheme as the dominating error source of our results, while the combined error in ME14 is slightly above our measurement error. The dominating S_0 uncertainty is also evident in Fig. 10 (a,b,c), where the spatial features of the combined error-grid are predominately determined by the S_0 grid. We find that the low accumulation zone at the northern slopes of PIG, which is next to the main trunk between

375 iSTAR site 1 to 6, shows combined S_0 patches that considerably exceed 100%. In contrast, combined error estimates in ME14 do not exceed 20% at the same location.

Initial tests on our OLK setting revealed that the choice of the negative kriging weights correction method has a noticeable
Figure 10. (a) Interpolation standard deviation S_0 of Fig. 8(a). (f) Measurement error of Fig. 8(a). (c) Root sum square of (a,b). (d) Varying PIG basin definitions according to Zwally et al. (2012), Fretwell et al. (2013), and Mouginot et al. (2017). Surface flow speeds adopted from Fig. 1. Background imagery taken from U.S., Geological Survey (2007) for all panels.
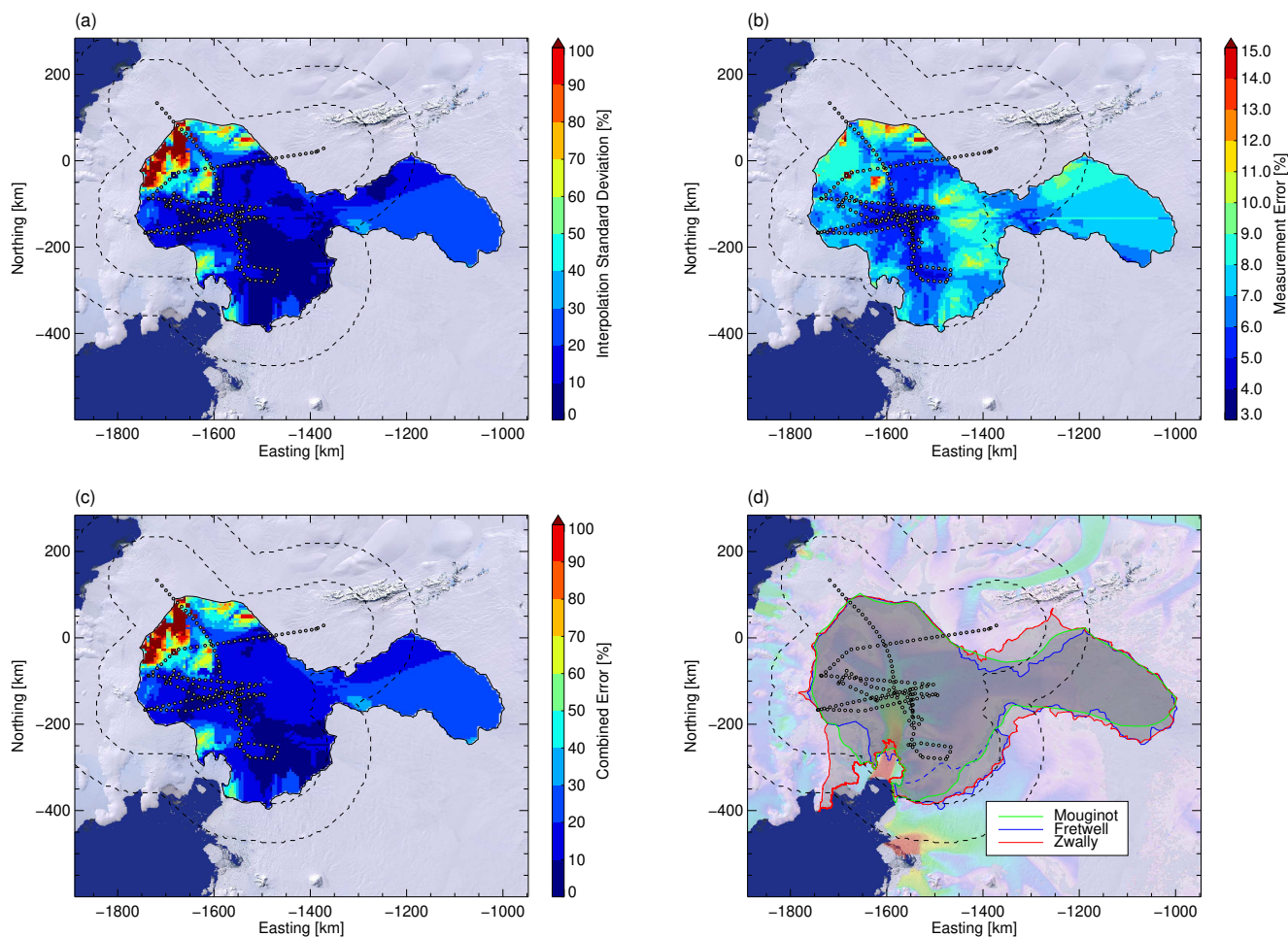
impact on the uncertainty estimates, a finding, which according to our knowledge, has not been reported before. However, our applied method by Deutsch (1996) already yields the minimum uncertainty estimates for our results, whereas the additional methods cited in Yamamoto (2000) yields an additional uncertainty increase between 20% (Froidevaux, 1993) and 50% (Journel and Rao, 1996).

Additional tests, where we used the kriging standard deviation based on non-transformed OK estimates, did not improve our interpolation uncertainty. Therefore the different choice of the interpolation uncertainty measure is not the source of the larger uncertainty range of this study. We hypothesize that despite the homoscedastic (i.e. data value independent) nature of the krige standard deviation, the reduction of data variance after subtracting the regression surface according to ME14 is most likely the

cause of their significantly lower uncertainty estimates.

In addition to the larger uncertainty range of this study, we note that the choice between cell-by-cell summation and RSS of grid errors has a quite substantial impact on the Σ_+ uncertainty estimates. If we make the optimistic assumption that gridded errors are independent and choose the calculation of RSS instead, Σ_+ uncertainty estimates would reduce to $\pm 0.5 \, \mathrm{Gt \, yr^{-1}}$

390   (i.e. $\sim 97\%$ less) for the combined Pine Island and Wedge basin.

4.4 Systematic retrieval impacts

In addition to the uncertainty assessment in section 4.3, we evaluated the impact of artificial cluster removal, the choice of the permittivity model, and the non-transformed OK scheme.

Artifical cluster removal

395   Inspection of the artificial cluster highlighted in Fig. 5 revealed that it is centred around the location with the lowest observed SMB and is essentially generated by the local nonbias terms of the OLK procedure. Owing to its steep contrast with the surroundings, it appears to be plausible to replace this cluster by averaged values of its nearest neighbours. However, due to the limited extend of this cluster, its additional contribution to the Σ_+ estimates would be less than 0.8%. Similarly, the impact on the PP-plot is negligible. Increasing the translational constant C helps removing this cluster, but at the cost of statistical

400   agreement between observations and estimates.

Looyenga based results

Defining ϵ' by Eq. (2) instead of Eq. (1) yields a minor reduction of Σ_+ for the PIG catchment of 0.6%, which we expect from Sinisalo et al. (2013). However, despite the minor impact of the alternative definition for ϵ', we noticed an additional small impact on the layer dating, which shifted our estimated layer formation from November to September 2004. Thus, we

405   had to adjust the time range in the RACMO SMB extraction for the calculation of hybrid SMB estimates. While the choice of the ϵ' model only has a minor impact on our total mass input estimates, it is worth noting that the effect on our annual layer dating is detectable.

Non-transformed kriging results

If we choose the OK procedure instead, Σ_+ increases by 4% for the Pine Island and 12% for the Wedge zone outlines, which

410   would further increase the offset between this study and ME14. However, inspection of the SMB distribution (not shown) indicates that estimates tend to overshoot near the coastline of the Amundsen Sea, which becomes particularly evident for the Wedge outlines. Hence, the OK procedure appears to be more sensitive to the limited observational constraints near the Wedge outlines. In addition, S_0 based uncertainty estimates increase by 27% and 88% for the Pine Island and Wedge outlines, which highlights the improved performance of the OLK procedure.

5   Conclusions

Our analysis provides updated mean annual SMB estimates for the PIG basin and 2005–2014 averaging period based on
a comprehensive airborne radar and ground truthing survey and complementary model simulations. Based on these estimates,
we calculated a total mass input of $79.9 \pm 19.2\ \mathrm{Gt\,yr^{-1}}$ for the PIG basin area. In comparison with earlier estimates from
airborne radar observations, which consider the 1985–2009 averaging period, our result shows 2% greater total mass input.
Given the uncertainty in both values, there is no significant difference between them. Hence, no distinct secular trend is visible
between both averaging periods. We conclude that our results provide further evidence that the recent total mass input can
be considered stationary at decadal scales. This implies that the increased dynamic ice loss over past decades remains the
driving force in the recent mass balance evolution of PIG. However, departures between both observations at the northern
slopes and southward interior of PIG may indicate temporal changes in the local SMB distribution, which cancel out for the
estimates on total mass input. Furthermore, our radar based observations can resolve a discrepancy between strainrate and SMB
measurement at iSTAR site 2, which highlights the benefit of such complementary SMB measurements for future missions.
Despite the minor changes in total mass input between both studies, the more than twofold uncertainty range of our results
remains striking. Neither can the applied model for the wave propagation speed of radar soundings nor the uncertainty related to
the regional density profile explain the larger uncertainty of this study. The same also applies for the reduced temporal averaging
time. A comprehensive evaluation of our uncertainty estimation revealed that assumptions on the geostatistical interpolation
error as well as grid-error dependences can have a substantial impact on the uncertainty estimation. In terms of the error
partitioning, our interpolation error is the dominating source of combined grid-errors. Moreover, varying basin definitions
have an impact on our total mass input estimate by up to 19%. This highlights the importance of a thorough documentation
of uncertainty estimates and basin definitions to improve future intercomparisons between different SMB and mass balance
inventories.

Data availability.   data submission to PANGAEA (in preparation)

Appendix A

A1

Author contributions.   S.Kowalewski conceived of the presented idea, designed the computational framework, adapted and tested the geo-
statistical krige methods, accomplished the reflection layer tracing in large parts, reprocessed the Neutron Probe density profiles for the data
calibration, wrote the manuscript with input from all authors, V. Helm performed the SAR level_1b ASIRAS data processing, provided the
digital elevation model, and established access to the RACMO2.3p2 data, E. Morris delivered the Neutron Probe density profiles, and O.
Eisen contributed to layer analysis and interpretation. All authors discussed the results and contributed to revising the manuscript.

Competing interests. Olaf Eisen is co-editor in chief of The Cryosphere

445   *Acknowledgements.* The German Ministry of Economics and Technology (grant 50EE1331 to S. Kowalewski) and European Space Agency (ESA) have supported this work as part of the CryoSat validation program. The authors gratefully acknowledge the excellent logistical support provided by British Antarctic Survey's (BAS) Rothera Research Station and members of the iSTAR Traverse and Alfred Wegener Institute during the field campaign, which has been funded by the UK Natural Environment Research Council, NERC grant NE/J005681/1. The authors express their gratitude towards A. Shepherd, PI of iSTAR-D project, for his general support and data contribution to this study.

450   The authors thank R. Mulvaney (BAS, UK) and H. Konrad (CPOM, University of Leeds, UK and DWD, Germany), for provision of datasets and discussions in an early stage. The authors gratefully acknowledge the provision of RACMO2.3p2 model output by S. Ligtenberg and M. van Wessem (IMAU, Utrecht University, NL). The authors would like to thank Emerson E&P Software, Emerson Automation Solutions, for providing licenses in the scope of the Emerson Academic Program.

References

455   Arcone, S. A., Spikes, V. B., Hamilton, G. S., and Mayewski, P. A.: Stratigraphic continuity in 400MHz short-pulse radar profiles of firn in West Antarctica, Annals of Glaciology, 39, 195–200, https://doi.org/10.3189/172756404781813925, 2004.

Bamber, J. L. and Dawson, G. J.: Complex evolving patterns of mass loss from Antarctica's largest glacier, Nature Geoscience, 13, 127–131, https://doi.org/10.1038/s41561-019-0527-z, 2020.

Deutsch, C. V.: Correcting for negative weights in ordinary kriging, Computers & Geosciences, 22, 765–773, https://doi.org/10.1016/0098-
460   3004(96)00005-2, 1996.

Eisen, O., Wilhelms, F., Nixdorf, U., and Miller, H.: Revealing the nature of radar reflections in ice: DEP-based FDTD forward modeling, Geophysical Research Letters, 30, https://doi.org/10.1029/2002gl016403, 2003.

Eisen, O., Frezzotti, M., Genthon, C., Isaksson, E., Magand, O., van den Broeke, M. R., Dixon, D. A., Ekaykin, A., Holmlund, P., Kameda, T., Karlöf, L., Kaspari, S., Lipenkov, V. Y., Oerter, H., Takahashi, S., and Vaughan, D. G.: Ground-based measurements of spatial and
465   temporal variability of snow accumulation in East Antarctica, Reviews of Geophysics, 46, –, https://doi.org/10.1029/2006RG000218, 2008.

Evans, S.: Dielectric Properties of Ice and Snow-a Review, Journal of Glaciology, 5, 773–792, https://doi.org/10.3189/s0022143000018840, https://www.cambridge.org/core/article/dielectric-properties-of-ice-and-snowa-review/A4F950358E513838DAE111F6A07EC077, 1965.

470   Fretwell, P., Pritchard, H. D., Vaughan, D. G., Bamber, J. L., Barrand, N. E., Bell, R., Bianchi, C., Bingham, R. G., Blankenship, D. D., Casassa, G., Catania, G., Callens, D., Conway, H., Cook, A. J., Corr, H. F. J., Damaske, D., Damm, V., Ferraccioli, F., Forsberg, R., Fujita, S., Gim, Y., Gogineni, P., Griggs, J. A., Hindmarsh, R. C. A., Holmlund, P., Holt, J. W., Jacobel, R. W., Jenkins, A., Jokat, W., Jordan, T., King, E. C., Kohler, J., Krabill, W., Riger-Kusk, M., Langley, K. A., Leitchenkov, G., Leuschen, C., Luyendyk, B. P., Matsuoka, K., Mouginot, J., Nitsche, F. O., Nogi, Y., Nost, O. A., Popov, S. V., Rignot, E., Rippin, D. M., Rivera, A., Roberts, J., Ross, N., Siegert, M. J.,
475   Smith, A. M., Steinhage, D., Studinger, M., Sun, B., Tinto, B. K., Welch, B. C., Wilson, D., Young, D. A., Xiangbin, C., and Zirizzotti, A.: Bedmap2: improved ice bed, surface and thickness datasets for Antarctica, The Cryosphere, 7, 375–393, https://doi.org/10.5194/tc-7-375-2013, 2013.

Froidevaux, R.: Constrained kriging as an estimator of local distribution functions., in: Proceedings of the International Workshop on Statistics of Spatial Processes: Theory and Applications., edited by Capasso, V., Girone, G., and Posa, D., pp. 106–118, Bari, Italia, 1993.

480   Gardner, A. S., Moholdt, G., Scambos, T., Fahnstock, M., Ligtenberg, S., van den Broeke, M., and Nilsson, J.: Increased West Antarctic and unchanged East Antarctic ice discharge over the last 7 years, The Cryosphere, 12, 521–547, https://doi.org/10.5194/tc-12-521-2018, 2018.

Hawley, R. L., M., M. E., Cullen, R., Nixdorf, U., Shepherd, A. P., and Wingham, D. J.: ASIRAS airborne radar resolves internal annual layers in the dry-snow zone of Greenland, Geophysical Research Letters, 33, –, https://doi.org/10.1029/2005GL025147, 2006.

Helm, V., Humbert, A., and Miller, H.: Elevation and elevation change of Greenland and Antarctica derived from CryoSat-2, The Cryosphere,
485   8, 1539–1559, https://doi.org/10.5194/tc-8-1539-2014, 2014.

Hillenbrand, C.-D., Smith, J. A., Hodell, D. A., Greaves, M., Poole, C. R., Kender, S., Williams, M., Andersen, T. J., Jernas, P. E., Elderfield, H., Klages, J. P., Roberts, S. J., Gohl, K., Larter, R. D., and Kuhn, G.: West Antarctic Ice Sheet retreat driven by Holocene warm water incursions, Nature, 547, 43–, https://doi.org/10.1038/nature22995, 2017.

Isaaks, E. H. and Srivastava, R. M.: An Introduction to Applied Geostatistic, Computers & Geosciences, 17, 471–473,
490   https://doi.org/10.1016/0098-3004(91)90055-I, 1991.

Journel, A. G. and Rao, S. E.: Deriving conditional distributions from ordinary kriging, Tech. Rep. 9, Stanford Center for Reservoir Fore-
casting, Stanford, 1996.

Konrad, H., Gilbert, L., Cornford, S. L., Payne, A., Hogg, A., Muir, A., and Shepherd, A.: Uneven onset and pace of ice-dynamical imbalance
in the Amundsen Sea Embayment, West Antarctica, Geophysical Research Letters, 44, 910–918, https://doi.org/10.1002/2016gl070733,
2017.

Konrad, H., Hogg, A. E., Mulvaney, R., Arthern, R., Tuckwell, R. J., Medley, B., and Shepherd, A.: Observations of surface mass bal-
ance on Pine Island Glacier, West Antarctica, and the effect of strain history in fast-flowing sections, Journal of Glaciology, pp. 1–10,
https://doi.org/10.1017/jog.2019.36, 2019.

Kovacs, A., Gow, A. J., and Morey, R. M.: The in-situ dielectric constant of polar firn revisited, Cold Regions Science and Technology, 23,
245–256, https://doi.org/10.1016/0165-232X(94)00016-Q, 1995.

Laepple, T., Hörhold, M., Münch, T., Freitag, J., Wegner, A., and Kipfstuhl, S.: Layering of surface snow and firn at Kohnen Station,
Antarctica: Noise or seasonal signal?, Journal of Geophysical Research: Earth Surface, 121, https://doi.org/10.1002/2016JF003919, 2016.

Lenaerts, J. T. M., van den Broeke, M. R., van de Berg, W. J., van Meijgaard, E., and Kuipers Munneke, P.: A new, high-resolution sur-
face mass balance map of Antarctica (1979-2010) based on regional atmospheric climate modeling, Geophysical Research Letters, 39,
https://doi.org/10.1029/2011gl050713, 2012.

Looyenga, H.: Dielectric constants of heterogeneous mixtures, Physica, 31, 401–406, https://doi.org/10.1016/0031-8914(65)90045-5, 1965.

Mavrocordatos, C., Attema, E., Davidson, M., Lentz, H., and Nixdorf, U.: Development of ASIRAS (Airborne SAR/Interferometric Al-
timeter System), in: IGARSS 2004. 2004 IEEE International Geoscience and Remote Sensing Symposium, vol. 4, pp. 2465–2467 vol.4,
https://doi.org/10.1109/IGARSS.2004.1369792, 2004.

Medley, B., Joughin, I., Das, S. B., Steig, E. J., Conway, H., Gogineni, S., Criscitiello, A. S., McConnell, J. R., Smith, B. E., Broeke,
M. R., Lenaerts, J. T. M., Bromwich, D. H., and Nicolas, J. P.: Airborne-radar and ice-core observations of annual snow accumulation
over Thwaites Glacier, West Antarctica confirm the spatiotemporal variability of global and regional atmospheric models, Geophysical
Research Letters, 40, 3649–3654, https://doi.org/10.1002/grl.50706, 2013.

Medley, B., Joughin, I., Smith, B. E., Das, S. B., Steig, E. J., Conway, H., Gogineni, S., Lewis, C., Criscitiello, A. S., McConnell, J. R.,
van den Broeke, M. R., Lenaerts, J. T. M., Bromwich, D. H., Nicolas, J. P., and Leuschen, C.: Constraining the recent mass balance of
Pine Island and Thwaites glaciers, West Antarctica, with airborne observations of snow accumulation, The Cryosphere, 8, 1375–1392,
https://doi.org/10.5194/tc-8-1375-2014, 2014.

Morris, E. M., Mulvaney, R., Arthern, R. J., Davies, D., Gurney, R. J., Lambert, P., De Rydt, J., Smith, A. M., Tuckwell, R. J., and Winstrup,
M.: Snow Densification and Recent Accumulation Along the iSTAR Traverse, Pine Island Glacier, Antarctica, Journal of Geophysical
Research: Earth Surface, 122, 2284–2301, https://doi.org/10.1002/2017JF004357, 2017.

Mouginot, J., Rignot, E., and Scheuchl, B.: Sustained increase in ice discharge from the Amundsen Sea Embayment, West Antarc-
tica, from 1973 to 2013, Geophysical Research Letters, 41, 1576–1584, https://doi.org/10.1002/2013GL059069, https://doi.org/10.1002/
2013GL059069, 2014.

Mouginot, J., Scheuchl, B., and Rignot, E.: MEaSUREs Antarctic Boundaries for IPY 2007-2009 from Satellite Radar, Version 2, Sub-
set: Basins_Antarctica_v02, Boulder, Colorado USA. NASA National Snow and Ice Data Center Distributed Active Archive Center,
https://doi.org/10.5067/AXE4121732AD [Date Accessed: 12/28/2019], 2017.

Overly, T. B., Hawley, R. L., Helm, V., Morris, E. M., and Chaudhary, R. N.: Greenland annual accumulation along the EGIG line, 1959–2004, from ASIRAS airborne radar and neutron-probe density measurements, The Cryosphere, 10, 1679–1694, https://doi.org/10.5194/tc-10-1679-2016, 2016.

530   Richardson, C., Aarholt, E., Hamran, S.-E., Holmlund, P., and Isaksson, E.: Spatial distribution of snow in western Dronning Maud Land, East Antarctica, mapped by a ground-based snow radar, Journal of Geophysical Research: Solid Earth, 102, 20 343–20 353, https://doi.org/10.1029/97jb01441, 1997.

Rignot, E., Mouginot, J., and Scheuchl, B.: MEaSUREs InSAR-Based Antarctica Ice Velocity Map, Version 2, Boulder, Colorado USA. NASA National Snow and Ice Data Center Distributed Active Archive Center, https://doi.org/10.5067/D7GK8F5J8M8R, 2017.

535   Rignot, E., Mouginot, J., Scheuchl, B., van den Broeke, M., van Wessem, M. J., and Morlighem, M.: Four decades of Antarctic Ice Sheet mass balance from 1979–2017, Proceedings of the National Academy of Sciences, 116, 1095–1103, https://doi.org/10.1073/pnas.1812883116, 2019.

Sinisalo, A., Anschütz, H., Aasen, A. T., Langley, K., von Deschwanden, A., Kohler, J., Matsuoka, K., Hamran, S.-E., Øyan, M.-J., Schlosser, E., Hagen, J. O., Nøst, O. A., and Isaksson, E.: Surface mass balance on Fimbul ice shelf, East Antarctica: Comparison of field measure-

540   ments and large-scale studies, J. Geophys. Res. Atmos., 118, 11,625–11,635, https://doi.org/10.1002/jgrd.50875, 2013.

U.S., Geological Survey: Landsat Image Mosaic of Antarctica (LIMA), Tech. rep., http://pubs.er.usgs.gov/publication/fs20073116, 2007.

van Wessem, J. M., van de Berg, W. J., Noël, B. P. Y., van Meijgaard, E., Amory, C., Birnbaum, G., Jakobs, C. L., Krüger, K., Lenaerts, J. T. M., Lhermitte, S., Ligtenberg, S. R. M., Medley, B., Reijmer, C. H., van Tricht, K., Trusel, L. D., van Ulft, L. H., Wouters, B., Wuite, J., and van den Broeke, M. R.: Modelling the climate and surface mass balance of polar ice sheets using RACMO2 – Part 2: Antarctica

545   (1979–2016), The Cryosphere, 12, 1479–1498, https://doi.org/10.5194/tc-12-1479-2018, 2018.

Yamamoto: Assessing Uncertainties for Lognormal Kriging Estimates, in: Proceedings of the 8th International Symposium on Spatial Accuracy Assessment in Natural Resources and Environmental Sciences: Accuracy in geomatics, edited by Zhang, J. and Goodchild, M. F., Spacial accuracy 2008, pp. 62–69, World Academic Union (World Academic Press), Shanghai, P. R. China, 2008.

Yamamoto, J.: An Alternative Measure of the Reliability of Ordinary Kriging Estimates, Mathematical Geology, 32, 489–509,

550   https://doi.org/10.1023/A:1007577916868, 2000.

Yamamoto, J.: Correcting the Smoothing Effect of Ordinary Kriging Estimates, Mathematical Geology, 37, 69–94, https://doi.org/10.1007/s11004-005-8748-7, 2005.

Yamamoto, J. K.: On unbiased backtransform of lognormal kriging estimates, Computational Geosciences, 11, 219–234, https://doi.org/10.1007/s10596-007-9046-x, 2007.

555   Zwally, H., Giovinetto, M. B., Beckley, M. A., and Saba, J. L.: Antarctic and Greenland Drainage Systems, GSFC Cryospheric Sciences Laboratory, https://doi.org/http://icesat4.gsfc.nasa.gov/cryo_data/ant_grn_drainage_systems.php, 2012.